

Impact of Fe(III) ions on the structural and optical properties of anatase-type solid solutions

Ivan Marić^a, Goran Dražić^b, Mile Ivanda^{c, d}, Tanja Jurkin^a, Goran Štefanić^{c, d, *}, Marijan Gotić^{c, d, *}

^a Radiation Chemistry and Dosimetry Laboratory, Ruder Bošković Institute, Bijenička c. 54, 10000, Zagreb, Croatia

^b National Institute of Chemistry, Hajdrihova 19, SI-1001, Ljubljana, Slovenia

^c Molecular Physics and New Materials Synthesis Laboratory, Ruder Bošković Institute, Bijenička c. 54, 10000, Zagreb, Croatia

^d Center of Excellence for Advanced Materials and Sensing Devices, Research Unit New Functional Materials, Bijenička c. 54, 10000, Zagreb, Croatia

ARTICLE INFO

Article history:

Received 4 October 2018

Received in revised form

5 November 2018

Accepted 5 November 2018

Available online 10 November 2018

Keywords:

Anatase

Fe-TiO₂

Band gap

Hematite

Iron doped TiO₂

XRD

Mössbauer

ABSTRACT

Iron/titanium oxide nanoparticles with the initial molar ratio $[\text{Fe}^{\text{III}}]/([\text{Fe}^{\text{III}} + \text{Ti}^{\text{IV}}]) \leq 0.50$ were hydrothermally synthesized at 180 °C in an aqueous ammonia solution ($\text{pH} \cong 9.6$). The titanium and iron precursors were TiCl_4 and FeCl_3 , respectively. The amount of doped iron strongly affected microstructural properties as well as the degree of dispersion of iron in the Fe-Ti-O system. Anatase was the dominant phase in the iron/titanium oxide samples with $[\text{Fe}/(\text{Fe} + \text{Ti})] \leq 0.25$. The average crystallite size of the anatase phase in iron/titanium oxide samples decreased with the increase of iron doping. The results of precise unit-cell parameters measurement, obtained using Rietveld refinements of the powder diffraction patterns with added silicon indicated that the solid solubility limit of Fe^{III} inside the anatase lattice was ~8 mol%. The appearance of hematite ($\alpha\text{-Fe}_2\text{O}_3$) sextet in the Mössbauer spectrum in the sample doped with 10 mol% of iron confirmed that the solid solubility limit of Fe^{III} in the TiO_2 lattice has been overreached. The relative concentrations of $\alpha\text{-Fe}_2\text{O}_3$ in the samples increased with Fe^{III} doping up to 15 mol% of added Fe^{III} and then, quite unexpectedly, the XRD 104 line and Mössbauer sextet of $\alpha\text{-Fe}_2\text{O}_3$ completely disappeared at $0.20 < [\text{Fe}/(\text{Fe} + \text{Ti})] < 0.30$. The EELS (electron energy-loss spectroscopy) analysis confirmed that the sample doped with 30 mol% of Fe^{III} contained no hematite. The Fe^{III} in the samples at $0.20 < [\text{Fe}/(\text{Fe} + \text{Ti})] < 0.30$ segregated not in the form of hematite, but in the form of iron/titanium oxide phase that was poorly crystallized or even amorphous. The $\alpha\text{-Fe}_2\text{O}_3$ again appeared at $[\text{Fe}/(\text{Fe} + \text{Ti})] = 0.50$. The diffuse reflectance spectra were used for band gap energy calculations. The band gap energy of the undoped TiO_2 sample was 3.1 eV, whereas the band gap energy of Fe-Ti-O samples doped with up to 10% showed a blue shift (3.2 eV). The significant red shift (from 3.2 to 2.4 eV) was observed in the samples with higher iron content (from 10 to 50 mol%).

© 2018 Elsevier B.V. All rights reserved.

1. Introduction

The incorporations of dopant cations have a significant impact on the structural, microstructural and catalytic properties of the obtained solid solutions. For example, the incorporation of up to 20 mol% of Fe^{III} stabilized high-temperature tetragonal polymer of zirconia, while the incorporation of more than 20 mol% of Fe^{III} stabilized cubic polymorph of zirconia [1–3]. Presence of divalent cations, such as Ni^{II} [4], Cu^{II} [5] or Zn^{II} [6] promoted sintering, while

the presence of tetravalent cations, such as Sn^{IV} , increased the porosity of the obtained material [7]. The incorporation of up to 3 mol% of Mg^{II} significantly increased the catalytic activity of ZrO_2 type solid solution in the catalytic oxidation of carbon monoxide [8]. The doping of TiO_2 with iron (Fe-Ti-O system) has been extensively investigated due to improving TiO_2 photocatalytic properties [9–11]. The undoped TiO_2 is a semiconductor with a band gap of about 3.0 eV and consequently, the UV light with wavelengths shorter than ~400 nm can generate electron-hole

* Corresponding authors. Molecular Physics and New Materials Synthesis Laboratory, Ruder Bošković Institute, Bijenička c. 54, 10000, Zagreb, Croatia.
E-mail addresses: Goran.Stefanic@irb.hr (G. Štefanić), gotic@irb.hr (M. Gotić).

pairs. The TiO₂ photogenerated holes and electrons can be used for the degradation of organic pollutants, water splitting, cancer treatment or self-cleaning surfaces [12–15]. It has been reported that iron doping shifts the absorption properties of TiO₂ into the visible part of the solar spectrum and improves the photocatalytic properties of undoped TiO₂ [16]. Schrauzer and Guth [17] reported the photoreduction of N₂ on the TiO₂ and iron-doped TiO₂ powders. Iron doping enhanced the photocatalytic activity for photochemical ammonia synthesis from N₂ and H₂O. Bahnemann [18] found that Fe-TiO₂ colloids showed higher yields for dichloroacetic acid photodegradation than undoped TiO₂. The highest quantitative yield was achieved for a compound containing 2.5 mol% of Fe. Choi et al. [19] have shown that iron doped TiO₂ significantly increased the photocatalytic activity for CCl₄ reduction and CHCl₃ oxidation. Ranjit et al. [20] reported an enhanced activity in the degradation of organic pollutants for iron (III)-phthalocyanine modified TiO₂ as compared to undoped TiO₂. Moniz et al. [21] photodeposited Fe₂O₃ on the P25 commercial TiO₂. The loading of Fe₂O₃ on TiO₂ was optimized and investigated for photocatalytic degradation of a model herbicide 2,4-dichlorophenoxyacetic acid (2,4-D) under solar irradiation. The photodeposited Fe₂O₃-P25 TiO₂ displayed a remarkable enhancement of more than 200% in the kinetics of complete mineralization of herbicide in comparison to the P25 TiO₂ photocatalyst. Ali et al. [22] synthesized the Fe-TiO₂ nanoparticles (NPs) with a dopant concentration from 0 to 10 mol% of iron. The synthesized Fe-doped TiO₂ nanoparticles effectively degrade methylene blue (MB) under visible-light illumination. The best photocatalytic activity showed the Fe-TiO₂ sample doped with 3.0 mol% of iron. In a previous work, we have shown that iron doped TiO₂ NPs possessed photocatalytic activity in the killing of cancer cells [23]. It was hypothesized that the enhanced photocatalytic activity of iron doped TiO₂ NPs in the killing of cancer cells in the presence UV irradiation might arise from the dissolution of iron, thus generating additional hydroxyl radicals by means of the photo Fenton and iron-catalyzed Haber-Weiss reactions.

Apart from the photocatalytic studies, an iron doped TiO₂ system is of a complex nature and its investigation is important from the structural standpoint [24,25]. The structural complexity of an iron doped TiO₂ system arises from the different solubility of iron in the three polymorphic modifications of TiO₂; anatase, brookite and rutile that can be present in the synthesized samples. Depending on the synthesis route, the solubility limit of iron in anatase, brookite and rutile can vary due to the different crystallinity, nanoparticle size and the presence of TiO₂ amorphous phase. Hirano et al. [26] synthesized iron (III) doped TiO₂ by hydrothermal treatment and subsequent annealing in the temperature ranges from 400 to 1000 °C. The synthesized samples with the iron content of up to 65 mol% were detected as single phase anatase-type structure with no diffraction peaks that could be assigned to other phases. Uekawa et al. [27] prepared wide compositional Fe(III) doped anatase by oxidation of Fe_xTiS₂. They have found that iron was dissolved in anatase lattice up to 30 mol% and that the amount of dissolved iron also depended on the oxidation method. Yu et al. [28] described a method for preparation of iron doped TiO₂ nanoparticles as a support material for a CO oxidation catalyst. The samples were prepared by a gel-hydrothermal method and the samples doped with up to 12 at% of iron were composed only of anatase structure with no trace of segregated iron oxides. Bickley et al. [29] prepared iron doped TiO₂ by a co-precipitation method from aqueous precursors and ammonia solution, followed by calcination at various temperatures and by the impregnation method where the commercial TiO₂ was added to an aqueous solution of iron (III) nitrate followed by firing in the air at various temperatures. Phase

formation depended on the synthesis method and temperature, as exemplified by the fact that hematite, rutile and anatase phases were formed by the impregnation method, but with the co-precipitation method, only rutile was present at 923 °C and 5 at% iron added. Generally, the iron-doped samples produced by the precipitation of mixed hydroxide from the solution of inorganic salts, or by hydrolysis from the corresponding alkoxides showed better homogeneity than the samples produced by the impregnation method. In our previous work [30], a series of iron/titanium oxide nanoparticles with Fe/Ti molar ratios up to 0.15 were synthesized by a modified sol-gel technique using Ti(IV)-isopropoxide and anhydrous Fe(II)-acetate. The precursors were mixed and subsequently hydrolyzed with water molecules generated *in situ* by an esterification reaction between acetic acid and ethanol. As-synthesized samples were amorphous for XRD, independent of the relative amount of doped iron. In order to obtain nanocrystalline iron/titanium oxide samples, as synthesized samples were calcinated at temperatures up to 800 °C. Iron that could not be incorporated in the anatase and rutile separated at higher heating temperatures (580 and 800 °C), in the forms of hematite (α -Fe₂O₃) and pseudobrookite (Fe₂TiO₅).

In this work, in order to avoid amorphous precursors and calcinations of as-synthesized samples, the nanocrystalline iron/titanium oxide particles were hydrothermally synthesized at 180 °C in aqueous ammonia solution (pH \approx 9.6). The titanium and iron precursors were TiCl₄ and FeCl₃, respectively. Choosing the same anion (Cl⁻) for titanium and iron precursor enabled similar precipitation behavior and good mixing of two different cations, as well as good dispersion of Fe^{III} in the TiO₂ matrix. Alkaline pH was selected in order to avoid brookite that could be formed at the acidic pH. Thus, under selected experimental conditions we obtained exclusively nanocrystalline anatase with no need for post-heating treatment, which enabled us to study the impact of Fe^{III} on the structural and optical properties of single-phase anatase-type solid solutions.

2. Experimental

2.1. Chemicals

TiCl₄ liquid (99%) supplied by Fluka, Cat No: 89545, HCl, 37% solution supplied by Fluka, Cat No: 258148, FeCl₃·6H₂O solid (99%) supplied by Sigma-Aldrich, Cat No: 31232-M, NH₃, 27% solution, p. a., supplied by Kemika, Zagreb.

2.2. Stock solution preparation

The 2 M HCl solution was prepared from concentrated HCl and then added to the TiCl₄ liquid. The HCl was added drop-wise to a round bottom flask containing 50 mL of TiCl₄ liquid through one of its four necks. The argon gas was bubbled during the addition of HCl solution to TiCl₄ liquid. Prior to the addition of TiCl₄ liquid to the flask, the liquid was cooled in an ice bath in order to limit the vigorous reaction of TiCl₄ with water. The concentration of the TiCl₄ stock solution was 2.5 mol dm⁻³ in 2.0 mol dm⁻³ HCl. The FeCl₃ solution was prepared by weighing 27.03 g of the solid FeCl₃·6H₂O and mixing it with 50 mL of deionized water in a volumetric flask. The calculated concentration of the iron stock solution was 2.0 mol dm⁻³ (2 M FeCl₃).

2.3. Synthesis

From previously prepared stock solutions, appropriate amounts

Table 1
The annotation of samples and corresponding volumes of 2.5 M TiCl₄ and 2.0 M FeCl₃ stock solutions added to the volumetric flask and filled with water up to the 50 mL mark. The [Fe^{III}/(Fe^{III} + Ti^{IV})] represents the molar fractions of initially added iron ions in precursor suspensions, whereas the $x_{\text{EDS}}(\text{Fe})$ represents the molar fraction of the iron (Fe) estimated from EDS measurements in powder samples.

Sample	V(TiCl ₄ stock solution) ^a /mL	V(FeCl ₃ stock solution) ^b /μL	[Fe ^{III} /(Fe ^{III} + Ti ^{IV})]	$x_{\text{EDS}}(\text{Fe})$
TiFe0	2.00	0	0.00	0.00
TiFe1	1.98	25	0.01	0.014
TiFe3	1.94	75	0.03	0.028
TiFe5	1.90	125	0.05	0.054
TiFe10	1.80	250	0.10	0.105
TiFe15	1.70	375	0.15	0.138
TiFe20	1.60	500	0.20	
TiFe25	1.50	625	0.25	0.232
TiFe30	1.40	750	0.30	
TiFe50	1.00	1250	0.50	0.503

^a The concentration of the TiCl₄ stock solution was 2.5 mol dm⁻³

^b The concentration of the FeCl₃ stock solution was 2.0 mol dm⁻³

of the aliquots were taken so that the molar ratio of iron and titanium ions in the mixture was from 0.00 up to 0.50 (Table 1). For example, the synthesis of TiO₂ sample doped with 10 mol % of Fe^{III}, i.e. at a ratio [Fe^{III}/(Fe^{III} + Ti^{IV})] = 0.10, the 250 μL of FeCl₃ stock solution was added to 1.80 mL of TiCl₄ stock solution. The aliquots were stirred in a volumetric flask and diluted with deionized water up to the 50 mL mark. The content of the flask was transferred to a 250 mL glass and the solution was stirred with a magnetic stirrer for few minutes. The pH of the solutions was measured using a pH-meter. With continuous stirring, concentrated solution of NH₃ (4 mL) was added drop-wise until the initial pH of solutions (the initial pH was 0.6–0.7 depending on the sample) increased up to 9.6–9.7. The magnet was removed from the glass and the newly formed precipitate was quantitatively transferred to a Teflon holder which was inserted in an autoclave. The steel autoclave was sealed, put into an oven and then heated for 24 h at 180 °C. After 24 h, the autoclave was removed from the oven, left to cool down naturally, and then opened. The pH of the mother liquor was measured (pH = 9.3–9.4). The sample was centrifuged and washed with water four times so that all impurities were removed. The wet samples were then dried in a vacuum dryer for 48 h.

2.4. Instrumental analysis

X-ray diffraction (XRD) measurements were performed at room temperature using APD 2000 diffractometer (CuKα radiation, graphite monochromator, NaI-Tl detector) manufactured by ITAL-STRUCTURES, Riva Del Garda, Italy.

Raman spectroscopy experiments were performed on a Horiba JobinYvon T64000 micro Raman system (laser wavelength of 514.5 nm). Accumulation times varied from 4 to 50 s. The experiments were done at room temperature and working power of 0.1 W.

Mössbauer spectra were collected in a transmission mode using standard instrumental configuration (WissEl GmbH, Starnberg, Germany). ⁵⁷Co in rhodium matrix was used as a source of radiation. The spectrometer was calibrated at room temperature using a standard spectrum of α-Fe foil.

Transmission electron microscopy of the samples was done on a Jeol ARM 200 CF microscope with voltage emission of 200 kV coupled with Gatan Quantum ER system for electron energy loss spectroscopy and energy dispersive x-ray spectrometry (Jeol Centurio 100).

Scanning electron microscopy was performed on a Jeol Ltd. 700F field-emission scanning electron microscope coupled with EDS/INCA 350 system for energy dispersive x-ray spectrometry

manufactured by Oxford Instruments Ltd.

UV–Vis spectra were collected with a Shimadzu UV/VIS/NIR spectrometer, model UV-3600. The used wavelength range was from 1200 to 300 nm.

Nitrogen adsorption measurements at 77 K for Brunauer–Emmett–Teller (BET) analysis and necessary degassing pre-treatment were done on Quantachrome Autosorb iQ3 system.

3. Results and discussions

Fig. 1 shows the results of the Rietveld refinements on powder diffraction patterns of samples TiFe0 to TiFe20. Silicon (Si) was used as an internal standard. The XRD lines of hematite (α-Fe₂O₃) and anatase TiO₂ phases, as well as XRD lines of silicon, are represented by small bars below the observed maxima. The R_{wp} values are below 8%, which indicate good quality of least squares refinement. The α-Fe₂O₃ segregated at [Fe/(Fe + Ti)] = 0.15 (sample TiFe15), which meant that the solubility limit of Fe^{III} in anatase TiO₂ was exceeded.

Fig. 2 shows the influence of the Fe^{III} content on crystal lattice parameters *a* and *c* (Å) and unit-cell volume (B) of the anatase TiO₂ solid solutions. The solubility limit of Fe^{III} in anatase lattice was estimated to 0.08 (8 mol%) using Rietveld and refinements of powder diffraction patterns. It should be noted here that the increase of the unit cell volume may arise from both the substitution of smaller Ti^{IV} (60.5 p.m.) with larger Fe^{III} (64.5 p.m.) in the lattice of anatase, as well as due to the decrease of anatase crystallite size with iron doping (Tables 2 and 4). The decrease of particle size introduces large lattice strain and more oxygen vacancies and as a consequence, the unit cell volume expands. For instance, Halistone et al. [31] have shown that the decrease of CeO₂ nanoparticle size from 11.8 to 1.1 nm was associated with the formation of oxygen vacancies (higher amounts of Ce^{III}), which led to larger lattice strain and a lattice parameter expansion of almost 7%.

The anatase TiO₂ and α-Fe₂O₃ (hematite) volume average domain sizes (Table 2) were estimated using Sherrer equation (Table 2):

$$D_v(hkl) = \frac{0.9\lambda}{\beta_{hkl} \times \cos \theta} \quad (1)$$

where $D_v(hkl)$ is a volume average domain sizes in the direction normal to the reflecting planes (*hkl*), λ is the x-ray wavelength (CuKα), θ is the Bragg angle and β_{hkl} is the pure full width of the diffraction line (*hkl*) at half the maximum intensity. The volume average domain sizes of anatase 101 line $D_v(101)$ decrease with

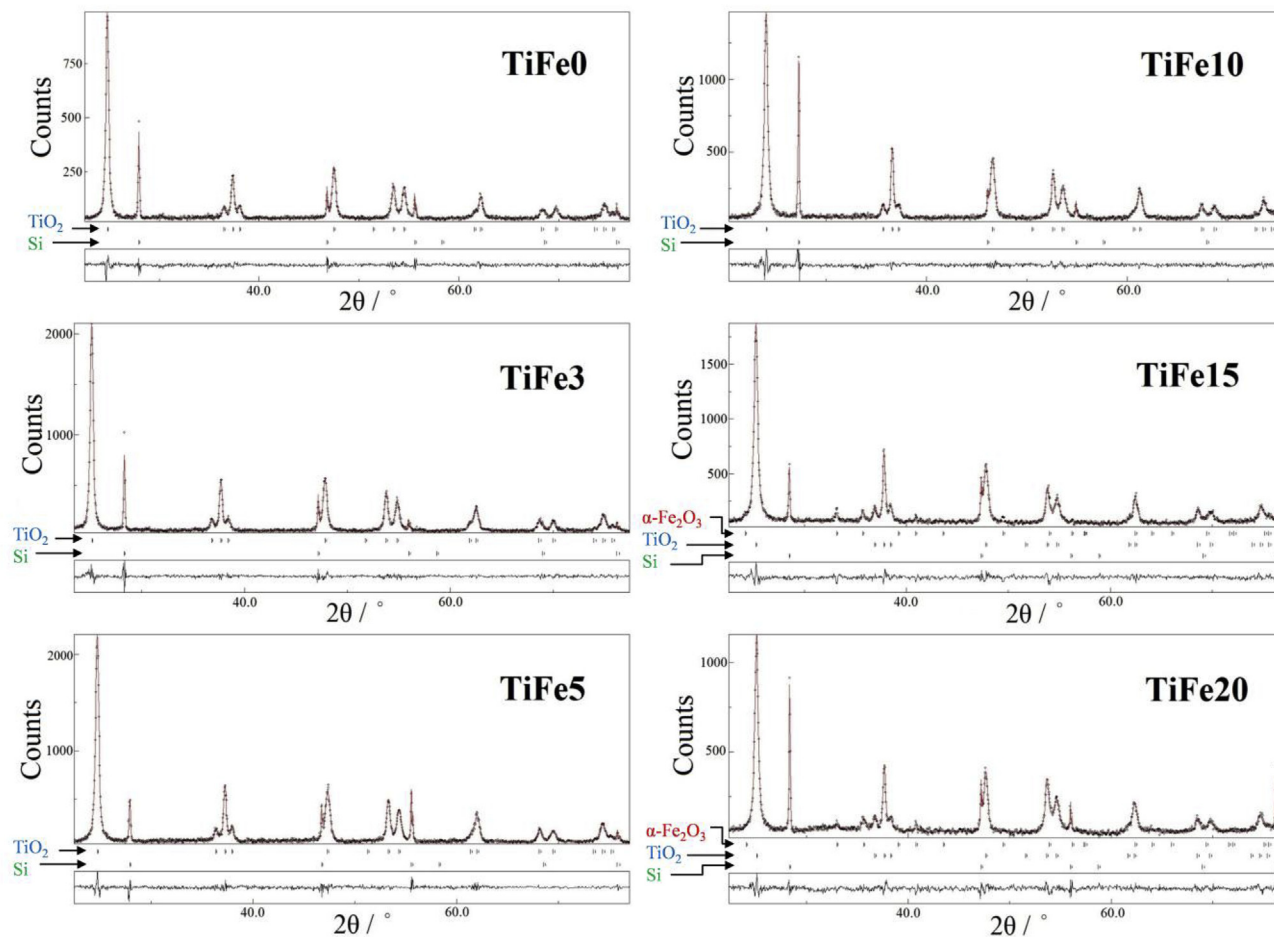


Fig. 1. The results of Rietveld refinements on powder diffraction patterns of samples TiFe0 to TiFe20. Silicon (Si) was used as an internal standard. The XRD lines of α -Fe₂O₃ and anatase TiO₂, as well as the XRD lines of silicon, are represented by small bars below the observed maxima. The difference between the observed and calculated patterns (R_{wp}) is shown as a line in the lower field. The R_{wp} values are below 8%, which indicate good quality of least squares refinement.

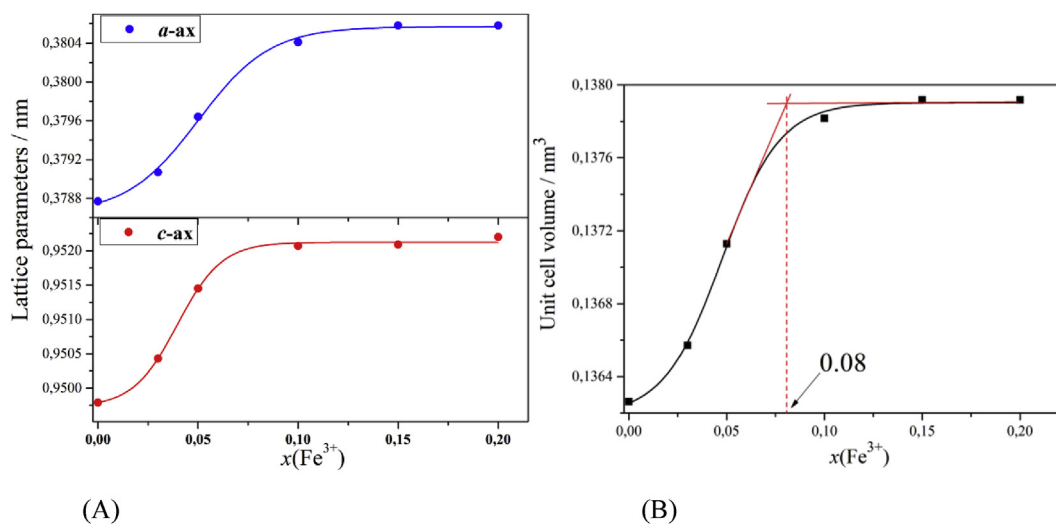


Fig. 2. The influence of the Fe^{III} content on crystal lattice parameters a and c (A) and unit-cell volume (B) of the anatase (TiO₂) solid solutions. The $x(\text{Fe}^{\text{III}})$ on the x-axis is the molar fraction of doped Fe^{III}. The value of 0.08 (8 mol %) represents the estimated solubility limit of Fe^{III} in anatase lattice.

iron doping from 22.5 nm (TiFe0) to 18.8 nm (TiFe15), but then again $D_v(101)$ increases to 23.8 nm in sample TiFe30. The sample

TiFe50 virtually had no anatase XRD lines. The XRD lines of hematite appeared at 15 mol% of added iron (sample TiFe15). The

Table 2
Results of line broadening analysis for samples TiFe0 to TiFe50. The volume average domain sizes D_v (hkl) were estimated using the Scherrer equation. The D_v (101) of anatase and D_v (104) and D_v (110) of hematite are given.

Sample	[Fe ^{III}]/(Fe ^{III} + Ti ^{IV})	Anatase			Hematite	
		a/nm	c/nm	D_v (101)/nm	D_v (104)/nm	D_v (110)/nm
TiFe0	0	0.37877 (1)	0.94979 (1)	22.5	–	–
TiFe3	0.03	0.37902 (1)	0.95043 (1)	22.5	–	–
TiFe5	0.05	0.37964 (1)	0.95145 (1)	19.7	–	–
TiFe10	0.10	0.38041 (1)	0.95207 (1)	19.0	–	–
TiFe15	0.15	0.38058 (1)	0.95209 (1)	18.8	46.8	32.0
TiFe20	0.20	0.38053 (1)	0.95219 (1)	19.3	–	17.4
TiFe25	0.25	–	–	22.0	–	14.4
TiFe30	0.30	0.38046 (1)	0.95200 (1)	23.8	–	13.8
TiFe50	0.50	–	–	–	15.0	16.0

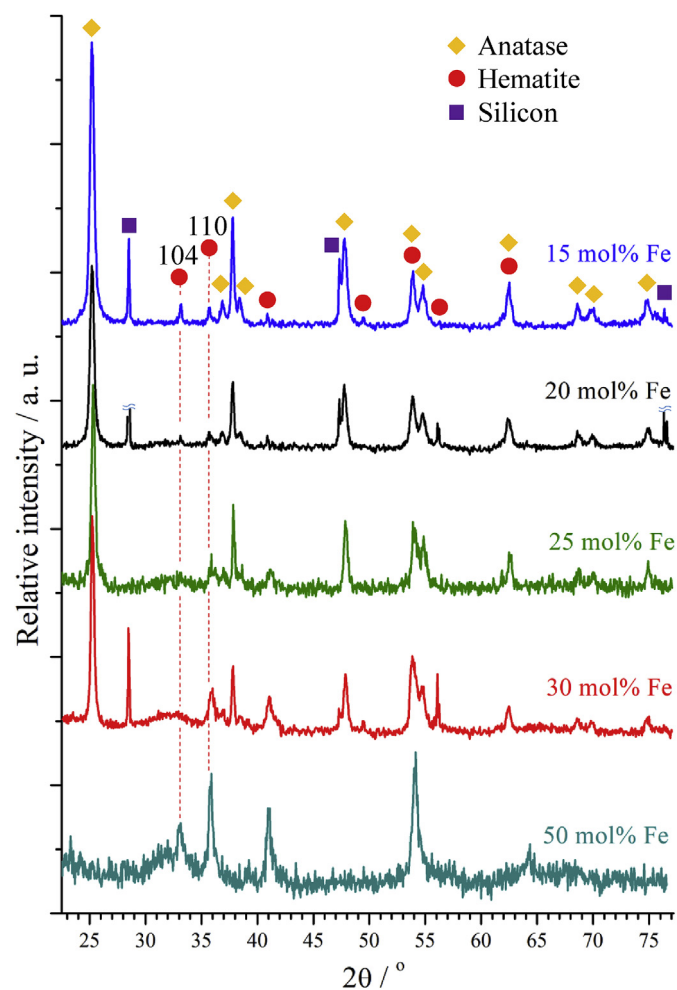


Fig. 3. XRD patterns showing 104 line of hematite visible in sample TiFe15 (15 mol % Fe^{III}) that gradually disappeared with Fe^{III} doping up to 30 mol % (TiFe30) and then again appeared in sample TiFe50 (50 mol % Fe^{III}).

values of D_v (104) and D_v (110) of hematite are given in Table 2. The D_v (110) decreases from 32.0 to 13.8 nm (samples TiFe15 to TiFe30), and then increases to 16.0 nm in sample TiFe50. The D_v (104) is 46.8 nm in sample TiFe15 and then 104 line unexpectedly disappears at 20, 25 and 30 mol% of doped Fe^{III} (Fig. 3). The 104 line in the sample TiFe50 again appeared, and D_v (104) has the lowest value of 15.0 nm.

Fig. 4 shows the Mössbauer spectra of samples TiFe1 to TiFe50. The Mössbauer parameters are given in Table 3. The samples TiFe1 and TiFe5 are characterized with a doublet that can be assigned to the paramagnetic high spin Fe^{III} incorporated in the crystal lattice of anatase TiO₂. The isomer shift (IS) and quadrupole splitting (QS) of this paramagnetic doublet (PD) are 0.37 and 0.66 mm s⁻¹, respectively. Sample TiFe10 is characterized by the superposition of a doublet and a sextet. The sextet H (red line) with hyperfine magnetic field (MF) of 50.80 T, QS of -0.18 mm s⁻¹, IS of 0.35 mm s⁻¹ and line width (LW) of 0.41 mm s⁻¹ is assigned to α -Fe₂O₃ (hematite) [32–34]. The relative abundance of α -Fe₂O₃ in sample TiFe10 is estimated to 13.7% by Mössbauer spectroscopy (Table 3). However, it is important to note that α -Fe₂O₃ was not identified by XRD in the same sample even though the solubility limit of Fe^{III} in anatase TiO₂ was estimated to 8 mol% using XRD. Mössbauer spectroscopy is sensitive only to iron (Fe), thus the result of 13.7% of α -Fe₂O₃ means that there is 13.7% of α -Fe₂O₃ relative to the total iron present in the sample. Since the sample TiFe10 has 10 mol% of initially added iron, the relative amount of α -Fe₂O₃ in sample TiFe10 is approximately only 1.4% and such a low quantity of α -Fe₂O₃ is not detectable by XRD (Fig. 1). The sextet that appeared in sample TiFe10 increased in sample TiFe15 and then quite unexpectedly disappeared in samples TiFe25 and TiFe30 (Fig. 4). The absence of hematite sextet in samples TiFe25 and TiFe30 is in accordance with XRD results, which show a broad amorphous maximum at the position of 104 line of hematite (Fig. 3). The hematite sextet again appeared in sample TiFe50, however, the high value of line width (LW = 0.64 mm s⁻¹) indicated broad particle size distribution.

The blue curve in Fig. 4 represents a doublet (D) due to the paramagnetic and/or superparamagnetic high spin Fe^{III} in an octahedral oxygen coordination. At low iron concentrations (samples TiFe1, TiFe3 and TiFe5) the Fe^{III} substitute the Ti^{IV} into the anatase crystal lattice and all Fe^{III} are in a paramagnetic state. At higher iron concentrations the Fe^{III} segregated as α -Fe₂O₃ (samples TiFe10, TiFe15 and TiFe50) that are characterized with sextet (magnetic hyperfine splitting) [33,35], however, the very small α -Fe₂O₃ NPs at room temperature may be in a superparamagnetic state [32,36–40]. The superparamagnetic nanoparticles show doublets in the Mössbauer spectrum at room temperature [35,40,41]. This is because at this relatively high temperature the thermal fluctuations become larger and more frequent, which cause the direction of magnetization to undergo random reorientation [42]. Thus, the doublet D in the samples with high concentration of Fe^{III} (samples TiFe10 to TiFe50) is due to the paramagnetic Fe^{III} (substitution of Fe for Ti in the anatase lattice) and/or very small superparamagnetic α -Fe₂O₃

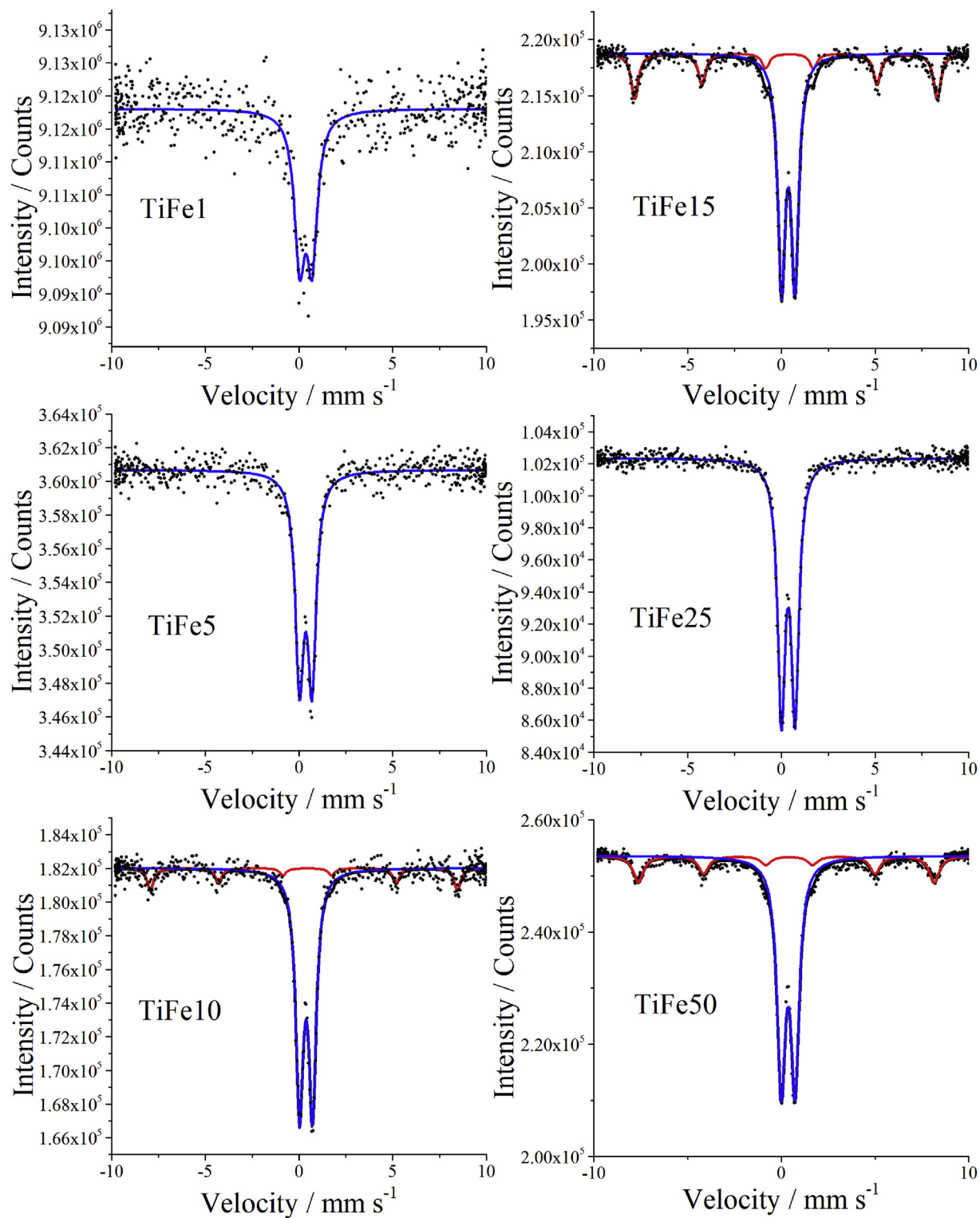


Fig. 4. Mössbauer spectra of samples TiFe1 to TiFe50. The blue curve represents the doublet due to the high spin Fe^{III} in an octahedral oxygen coordination, whereas the red curve represents the sextet due to the $\alpha\text{-Fe}_2\text{O}_3$ (hematite).

Table 3
 ^{57}Fe Mössbauer spectroscopy parameters for samples TiFe1 to TiFe50.

Sample	Fitting curve	$IS/\text{mm s}^{-1}$	$QS/\text{mm s}^{-1}$	MF/T	$LW/\text{mm s}^{-1}$	Relative area/%	Assignations	χ^2
TiFe1	D	0.37	0.66	–	0.68	100.0	Fe^{III} , PD	1.09
TiFe3	D	0.41	0.65	–	0.56	100.0	Fe^{III} , PD	1.12
TiFe5	D	0.36	0.66	–	0.54	100.0	Fe^{III} , PD	0.97
TiFe10	D	0.38	0.69	–	0.47	86.3	Fe^{III} , PD/SP	1.17
	H	0.35	–0.18	50.80	0.41	13.7	$\alpha\text{-Fe}_2\text{O}_3$	
TiFe15	D	0.37	0.72	–	0.46	71.5	Fe^{III} , PD/SP	1.18
	H	0.34	–0.19	50.06	0.46	28.5	$\alpha\text{-Fe}_2\text{O}_3$	
TiFe25	D	0.37	0.74	–	0.48	100.0	Fe^{III} , PD/SP	1.25
TiFe30	D	0.35	0.74	–	0.52	100.0	Fe^{III} , PD/SP	1.13
TiFe50	D	0.36	0.74	–	0.53	78.0	Fe^{III} , PD/SP	2.83
	H	0.34	–0.16	48.97	0.64	22.0	$\alpha\text{-Fe}_2\text{O}_3$	

IS = isomer shift relative to $\alpha\text{-Fe}$ at room temperature; QS = quadrupole splitting or quadrupole shift; MF = hyperfine magnetic field; LW = line width; PD = paramagnetic doublet; SP = superparamagnetic doublet; H = $\alpha\text{-Fe}_2\text{O}_3$ (hematite) sextet.

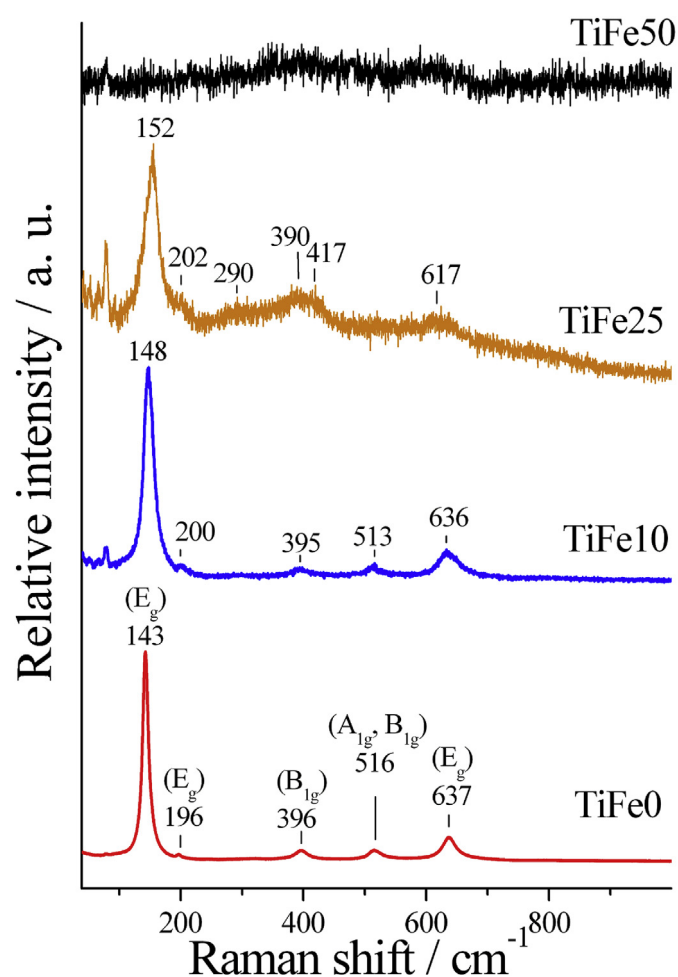


Fig. 5. Raman spectra of samples TiFe0, TiFe10, TiFe25 and TiFe50.

nanoparticles. The values of QS around 0.70 mm s^{-1} or higher (samples TiFe10 to TiFe50) suggest that these samples contain very small iron oxide nanoparticles with Fe^{III} in highly disordered local environments.

Fig. 5 shows Raman spectra of samples TiFe0, TiFe10, TiFe25 and TiFe50. The Raman bands of undoped TiO_2 sample (TiFe0) are in good agreement with the six allowed Raman modes of anatase; ν_6 (E_g) at 144 cm^{-1} ; ν_5 (E_g) at 197 cm^{-1} ; ν_4 (B_{1g}) at 399 cm^{-1} ; ν_3 (A_{1g})

at 513 cm^{-1} ; ν_2 (B_{1g}) 519 cm^{-1} ; and ν_1 (E_g) 639 cm^{-1} reported by Ohsaka et al. [43]. The modes of ν_1 (E_g) 639 cm^{-1} , ν_2 (B_{1g}) 519 cm^{-1} and ν_3 (A_{1g}) 513 cm^{-1} are the Ti-O bond stretching type vibrations, whereas the modes of ν_6 (E_g) 144 cm^{-1} ; ν_5 (E_g) 197 cm^{-1} ; ν_4 (B_{1g}) 399 cm^{-1} are the O-Ti-O bending type vibrations. The most intense band of anatase at 144 cm^{-1} shifted towards higher wavenumbers, it became broader and its intensity decreased with the increment of the Fe^{III} dopant. Raman spectrum of $\alpha\text{-Fe}_2\text{O}_3$ (hematite) exhibits seven bands at about 226 (A_{1g}), 245 (E_g), 293 (E_g), 298 (E_g), 412 (E_g), 500 (A_{1g}) and 612 (E_g) cm^{-1} [44,45]. The bands at 226 (A_{1g}) and 293 (E_g) cm^{-1} are the most intense hematite Raman bands. Thus, the new band at 290 cm^{-1} in sample TiFe25 can be associated with the Raman (E_g) mode of hematite. The absence of 104 XRD line of hematite in sample TiFe25 is not in contradiction with the observed hematite band at 290 cm^{-1} , because the Raman spectroscopy is much more sensitive to the Fe^{III} short-range order environment in comparison to XRD. The Raman spectrum of sample TiFe50 shows no visible Raman bands because of the high self-absorption of the laser beam (wavelength of 514.5 nm) by the red colored sample.

Fig. 6 shows SEM micrographs and corresponding particle size distributions of samples TiFe1 (a), TiFe5 (b), TiFe10 (c), TiFe15 (d), TiFe25 (e) and TiFe50 (f). The SEM image and corresponding particle size distribution of sample TiFe0 are shown in **Fig. S1** in the **Supplementary Material**. Generally, two trends are visible; the Fe^{III} doping causes the decrease in particle size up to 15 mol\% of Fe^{III} , and then the reverse effect is visible where the particle size increases from 38.0 nm in sample TiFe15 to 99.2 nm in sample TiFe50. The values of BET specific surface area are in agreement with these two trends (**Table 4**).

Fig. 7 shows TEM micrographs with particle size distributions (a, b) and corresponding EDS elemental mapping (c, d) of samples TiFe15 (a, c), TiFe30 (b, d). Sample TiFe15 consists of two types of particles, the smaller ones that have octahedral morphology and are about 20 nm in size are characteristic of anatase, whereas the bigger NPs of about 100 nm in size and hexagonal morphology are characteristic of hematite. The average particle size, taking into account both types of nanoparticles, is 26.1 nm . The EDS elemental mapping shows that small octahedrons are titanium-rich (a lot of red dots) and at the same time iron-poor (sparsely dispersed green dots). On the contrary, the big hexagon nanoparticles are iron-rich and contain exclusively iron (Fe) and oxygen (O).

Sample TiFe30 (**Fig. 7b**) also consists of two types of particles. The smaller ones, slightly irregular and elongated octahedrons, are about 30 nm in size. The bigger particles are of irregular morphology and about 100 nm in size. The mean particle size of

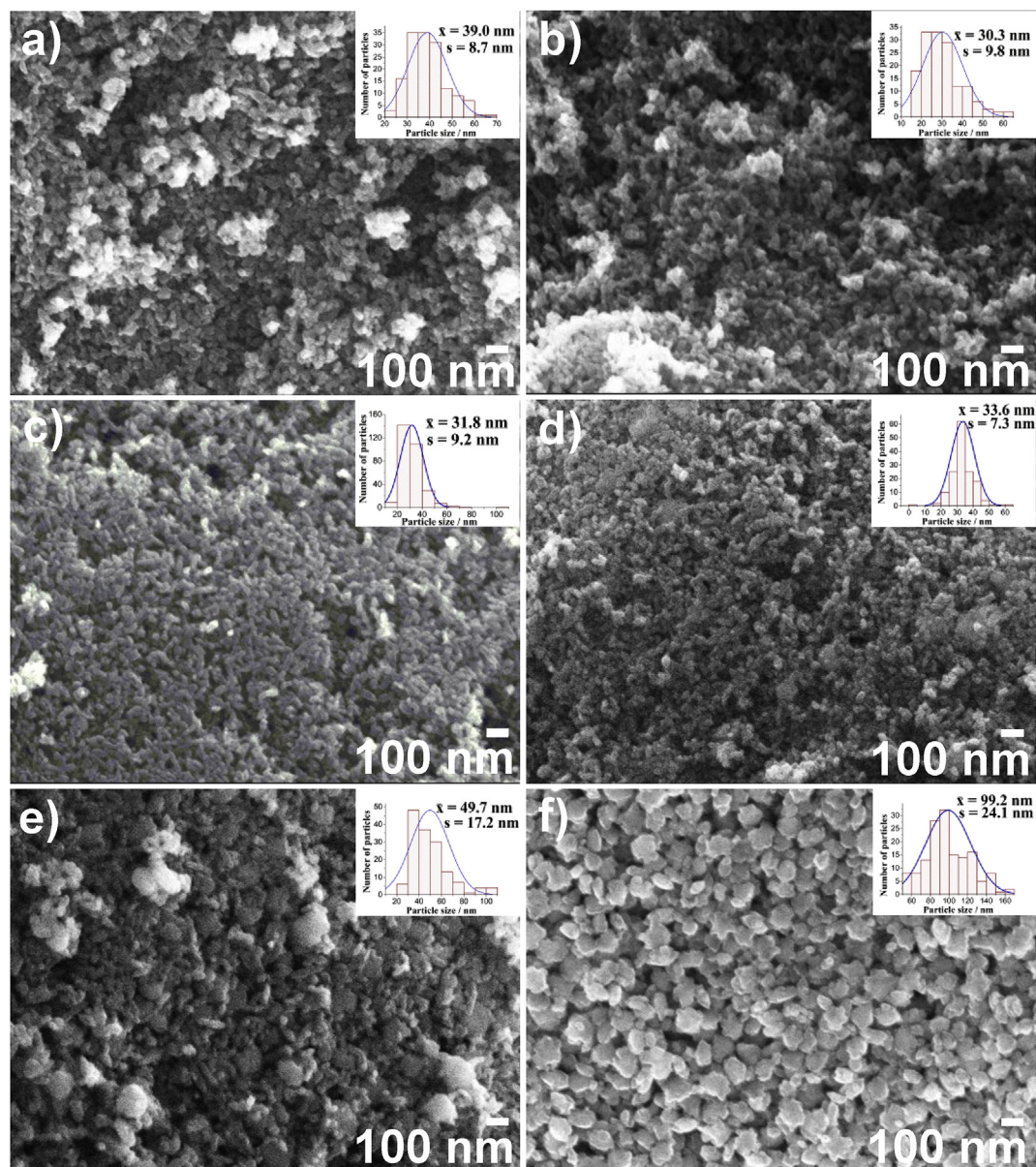


Fig. 6. SEM micrographs and corresponding particle size distributions of samples TiFe1 (a), TiFe5 (b), TiFe10 (c), TiFe15 (d), TiFe25 (e) and TiFe50 (f).

Table 4

SEM mean particle sizes and BET specific surface areas of samples TiFe0 to TiFe50.

Sample	SEM mean particle size/nm	BET specific surface area/m ² g ⁻¹
TiFe0	42.9	52.7
TiFe1	39.0	–
TiFe5	30.3	62.4
TiFe10	31.8	61.8
TiFe15	38.0	54.7
TiFe25	49.7	39.6
TiFe50	99.2	25.9

32.6 nm was calculated taking into account both types of particles. The EDS elemental mapping of sample TiFe30 (Fig. 7d) was done on

the rectangular area bordered by the dashed red line. The EDS mapping shows the iron and titanium-rich areas (particles on the right and at the top of Fig. 7b) and titanium-rich particles (particles on the left side of Fig. 7b), however, there are no exclusively iron-rich particles as in the case of sample TiFe15.

Fig. 8 shows STEM-ADF image and corresponding electron energy loss spectroscopy (EELS) analysis of sample TiFe15. EELS analysis was taken at the spots 1, 1a and 2. The hexagonal-like particle at the spot 1 and 1a consists of very high Fe L2 and L3 edge peaks, whereas the O-K edge and Ti L2 and L3 edge peaks are of much lower intensity. The particle at the spot 2 contains oxygen, a lot of titanium (Ti) and very small amount of iron (Fe). Therefore,

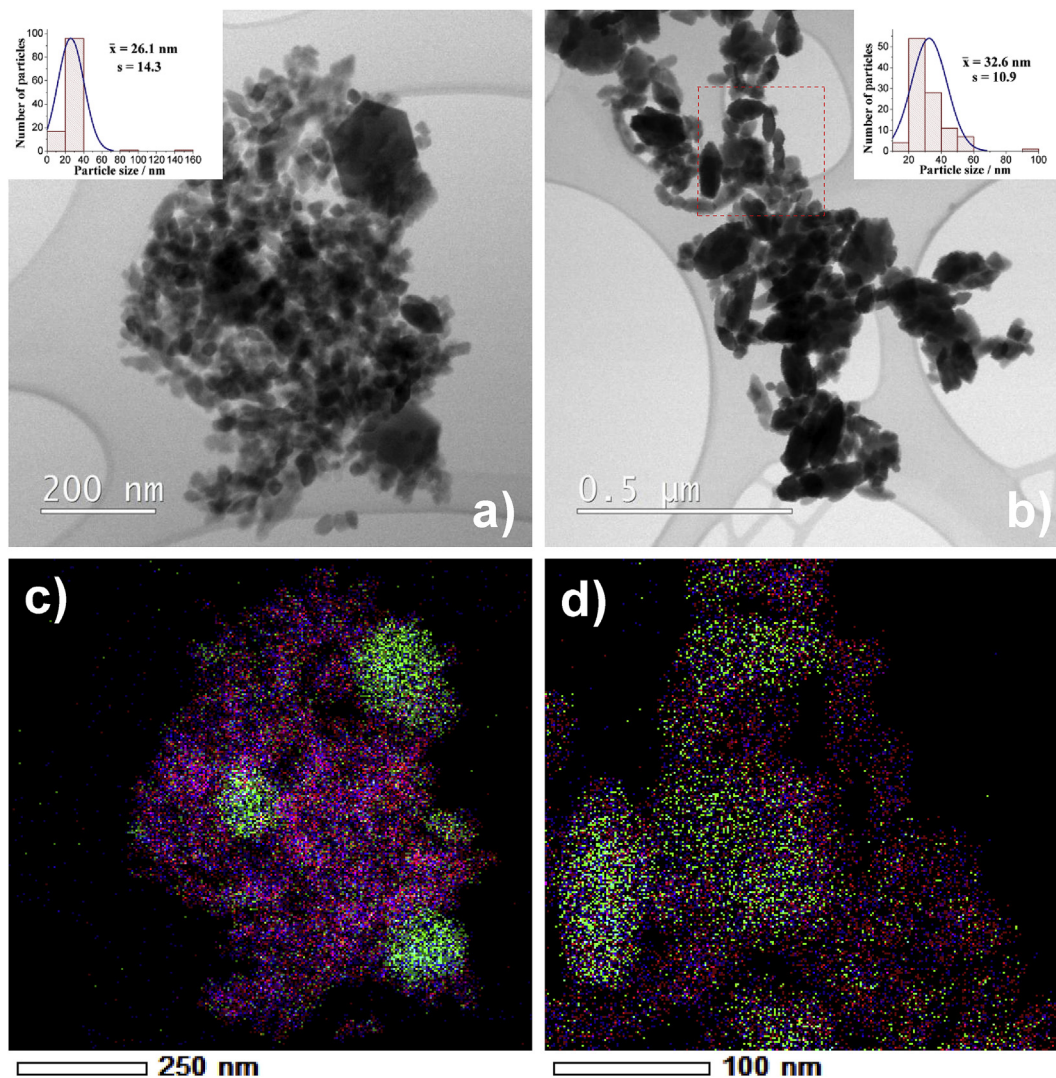


Fig. 7. TEM micrographs with particle size distributions (a, b) and corresponding EDS elemental mapping (c, d) of samples TiFe15 (a, c), TiFe30 (b, d); Green = Fe, blue = O, red = Ti.

sample TiFe15 consists of iron-rich particles with a small amount of titanium and of titanium-rich particles with a very small amount of iron. These results are in accordance with EDS results presented in Fig. 7b.

Fig. 9 shows STEM dark-field and STEM-ADF images as well as corresponding EELS analysis of sample TiFe30. The EELS analysis was taken at the spots 1 and 2. The octahedron particle at the spot 1 consists of titanium (Ti) and oxygen (O) with no iron (Fe), whereas the particle at spot 2 consists of titanium, oxygen and iron (Fe). Sample TiFe30 contains no highly loaded iron particles characteristic of hematite. Therefore, the EELS analysis in line with XRD results (Fig. 3) confirms that the sample TiFe30 contains no hematite. Obviously, in the sample TiFe30 the Fe^{III} segregated not in the form of hematite, but in the form of iron/titanium phase that was poorly crystallized or even amorphous (Fig. 2). Besides, in sample TiFe30 the titanium-rich octahedrons contained virtually no iron, which implied that iron expelled from anatase structure.

Fig. 10 shows Tauc plots of the synthesized samples, whereas the reflectance spectra are shown in Fig. S2 in the Supplementary Material. The band gap energy of samples was calculated based

on the Kubelka-Munk function. The following relation is used:

$$(h\nu\alpha)^{1/n} = A(h\nu - E_g) \quad (2)$$

where h is Planck's constant, ν is frequency, α is absorption coefficient, E_g is band gap and A is proportionality constant. The value of the exponent n represents the type of sample transition ($n = 2$ for indirect allowed transition, $n = 0.5$ for direct allowed transition). The calculations were performed for indirect band gap energy determination; therefore, the value of n was set to 2. The collected diffuse reflectance spectra were converted to the Kubelka-Munk function. The vertical axis was converted to a quantity $(h\nu F(R_\infty))^{1/2}$ where $F(R_\infty)$ is proportional to the absorption coefficient and is calculated by the following equation:

$$F(R_\infty) = (1 - R)^2 / 2R \quad (3)$$

where R is reflectance at a given wavelength. Using the calculated values, $(h\nu F(R_\infty))^{1/2}$ was plotted against $h\nu$. A line tangent to the linear part of the curve was drawn through the inflection point and

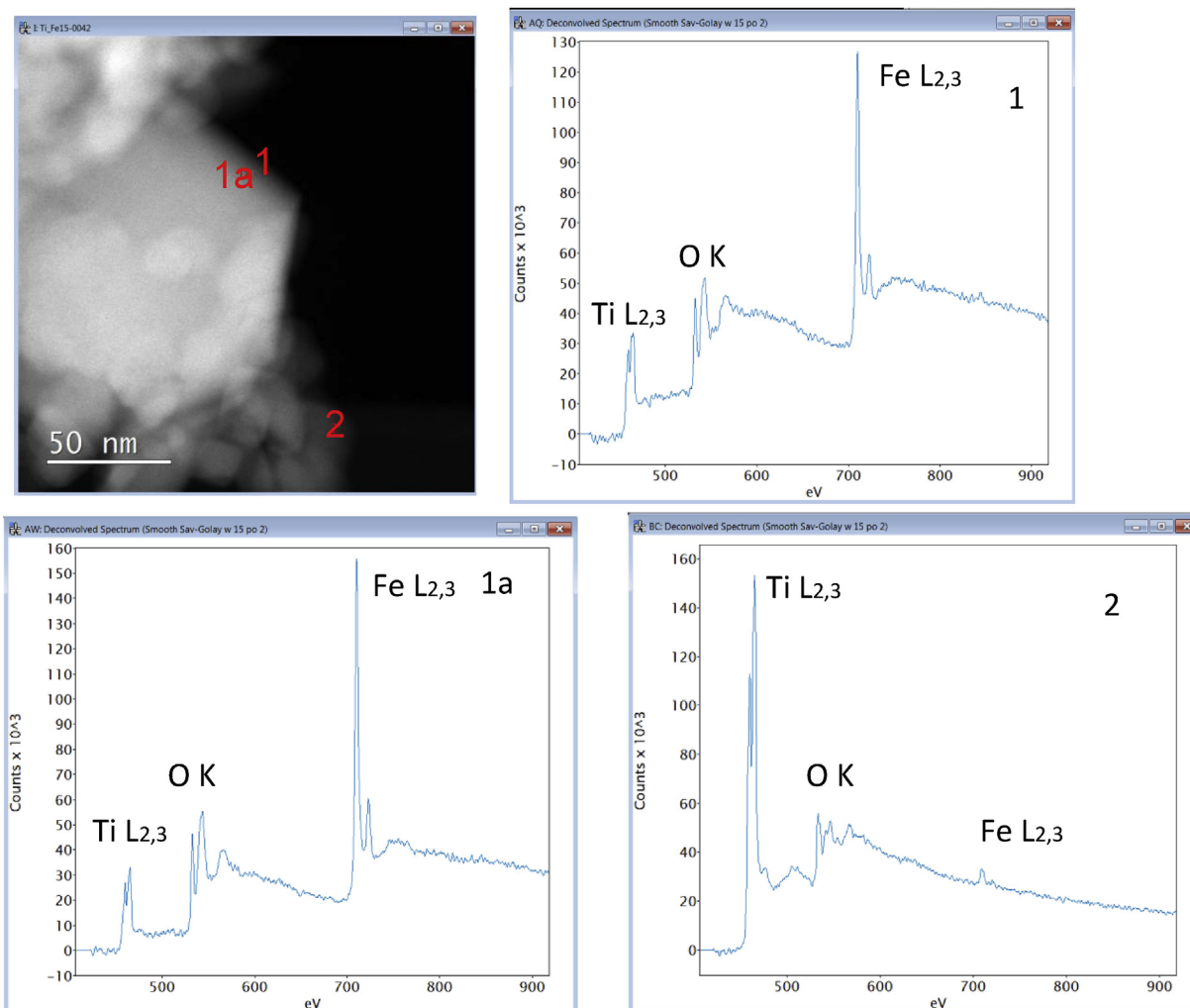


Fig. 8. STEM-ADF image and corresponding EELS (electron energy loss spectroscopy) analysis of sample TiFe15. EELS analysis was taken at the spots 1, 1a and 2. The hexagon-like particle at the spot 1 and 1a consists of very high Fe L2 and L3 edge peaks, whereas the O-K edge and Ti L2 and L3 edge peaks are of much lower intensity. The particle at the spot 2 contains oxygen, a lot of titanium (Ti) and very small amount of iron (Fe).

extrapolated to zero reflectance. Inflection points of the curves were found by taking the first derivative of the function and locating the point at which the value of the first derivative coefficient begins to decrease after increasing. A line tangent to the linear part of the curve was drawn through the inflection point and extrapolated to zero reflectance. The extrapolated value was taken as the band gap energy of the material.

The band gap energy of the undoped TiO₂ sample was 3.1 eV, whereas the band gap energy of Fe-Ti-O samples doped with up to 10 mol% of Fe^{III} showed a blue shift (3.2 eV). Therefore, in contrast to reports of other studies we have observed no red shift of the band gap energies to the visible part of the absorption solar spectrum within the solubility limit of Fe^{III} in anatase TiO₂ lattice. On the contrary, a significant red shift from 3.2 to 2.4 eV was observed in the samples with higher Fe^{III} content (from 10 to 50 mol% of doped Fe^{III}, Fig. S2 and Fig. 10).

4. Conclusions

We performed hydrothermal synthesis in order to obtain

nanocrystalline anatase as a single phase with no need for post-heating treatment, which enabled us to study the impact of Fe^{III} on the structural and optical properties of single-phase anatase-type solid solutions.

The solubility limit of Fe^{III} in anatase lattice was estimated to 8 mol% using Rietveld refinements of powder diffraction patterns. Fe^{III} that could not be dissolved in TiO₂ crystal lattice separated as α -Fe₂O₃ (up to 20 mol % and at 50 mol of doped Fe^{III}).

The relative concentrations of α -Fe₂O₃ in the samples increased up to 15 mol% of added Fe^{III} and then, quite unexpectedly, the XRD 104 line and Mössbauer sextet of α -Fe₂O₃ completely disappeared at $0.20 < [\text{Fe}/(\text{Fe} + \text{Ti})] < 0.30$, whereas at $[\text{Fe}/(\text{Fe} + \text{Ti})] = 0.50$ the α -Fe₂O₃ again appeared. The XRD and EELS results proved that sample TiFe30 contained no hematite and that iron in this sample segregated in the form of iron/titanium phase that was poorly crystalline or even amorphous (Figs. 3 and 9).

The band gap energy of the undoped TiO₂ sample was 3.1 eV, whereas the band gap energy of Fe-Ti-O samples doped with up to 10 mol% of Fe^{III} showed a blue shift (3.2 eV). The significant red shift from 3.2 to 2.4 eV was observed in the samples with higher Fe^{III}

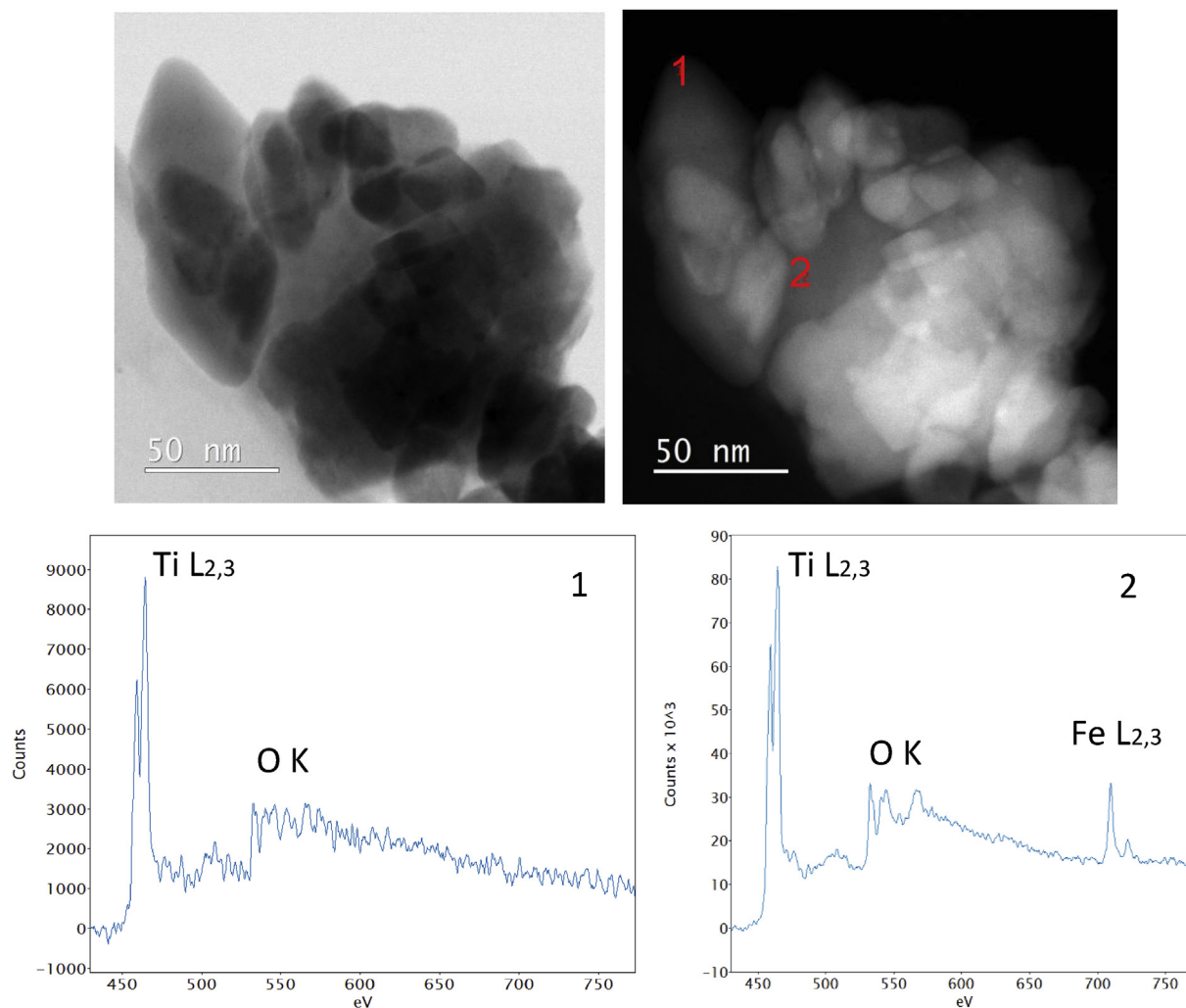


Fig. 9. STEM dark-field and STEM-ADF images as well as corresponding EELS (electron energy-loss spectroscopy) analysis of sample TiFe30. EELS analysis was taken at the spots 1 and 2. The octahedron particle at the spot 1 consists of titanium (Ti) and oxygen (O), whereas the particle at spot 2 consists of titanium, oxygen and iron (Fe).

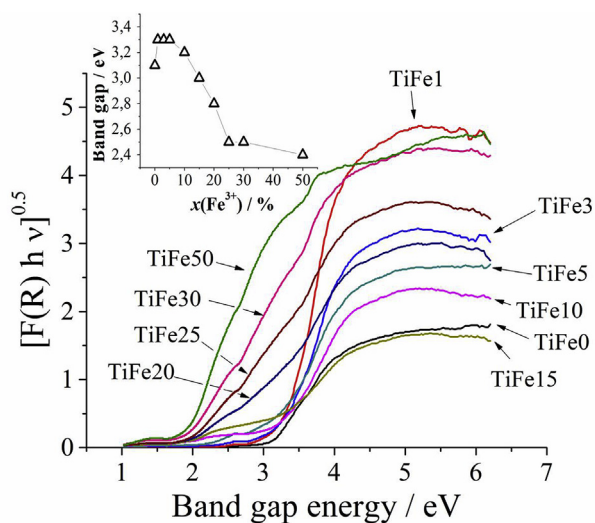


Fig. 10. Tauc plots of the synthesized samples and corresponding band gap values as a function of iron doping (inset).

content (from 10 to 50 mol %).

Acknowledgments

This work has been fully supported by a project co-financed by the Croatian Government and the European Union through the European Regional Development Fund - the Competitiveness and Cohesion Operational Programme (KK.01.1.1.01.0001). Financial support from the Slovenian Research Agency, the research program P2-0393 (Goran Dražić) is acknowledged. We also thank Mr. Jasmin Forić for the help in experimental work.

Appendix A. Supplementary data

Supplementary data to this article can be found online at <https://doi.org/10.1016/j.molstruc.2018.11.015>.

References

- [1] G. Štefanić, B. Gržeta, K. Nomura, R. Trojko, S. Musić, The influence of thermal treatment on phase development in ZrO_2 - Fe_2O_3 and HfO_2 - Fe_2O_3 systems, *J. Alloy. Comp.* 327 (2001) 151–160, [https://doi.org/10.1016/S0925-8388\(01](https://doi.org/10.1016/S0925-8388(01)

- 01401-3.
- [2] G. Štefanić, S. Musić, A. Gajović, Structural and microstructural changes in monoclinic ZrO₂ during the ball-milling with stainless steel assembly, *Mater. Res. Bull.* 41 (2006) 764–777, <https://doi.org/10.1016/j.materresbull.2005.10.006>.
 - [3] G. Štefanić, S. Musić, A. Gajović, A comparative study of the influence of milling media on the structural and microstructural changes in monoclinic ZrO₂, *J. Eur. Ceram. Soc.* 27 (2007) 1001–1016, <https://doi.org/10.1016/j.jeurceramsoc.2006.04.136>.
 - [4] G. Štefanić, M. Didović, S. Musić, The influence of thermal treatment on the phase development of ZrO₂–NiO precursors, *J. Mol. Struct.* 834 (2007) 435–444, <https://doi.org/10.1016/j.molstruc.2006.11.004>.
 - [5] G. Štefanić, S. Musić, M. Ivanda, Effect of Cu²⁺ ion incorporation on the phase development of ZrO₂-type solid solutions during the thermal treatments, *J. Alloy. Comp.* 491 (2010) 536–544, <https://doi.org/10.1016/j.jallcom.2009.10.263>.
 - [6] G. Štefanić, S. Musić, M. Ivanda, Phase development of the ZrO₂-ZnO system during the thermal treatments of amorphous precursors, *J. Mol. Struct.* 924–926 (2009) 225–234, <https://doi.org/10.1016/j.molstruc.2008.10.044>.
 - [7] G. Štefanić, S. Musić, M. Ivanda, Thermal behavior of the amorphous precursors of the ZrO₂-SnO₂ system, *Mater. Res. Bull.* 43 (2008) 2855–2871, <https://doi.org/10.1016/j.materresbull.2007.12.016>.
 - [8] V. Nemeč, H. Kaper, G. Pétaud, M. Ivanda, G. Štefanić, Impact of Mg²⁺ ion incorporation on the phase development of ZrO₂-type solid solutions and their application in the catalytic oxidation of carbon monoxide, *J. Mol. Struct.* 1140 (2017) 127–141, <https://doi.org/10.1016/j.molstruc.2016.12.088>.
 - [9] N.C. Birben, C.S. Uyguner-Demirel, S. Sen Kavurmaci, Y.Y. Gürkan, N. Turkten, Z. Cinar, M. Bekbolet, Application of Fe-doped TiO₂ specimens for the solar photocatalytic degradation of humic acid, *Catal. Today* 281 (2017) 78–84, <https://doi.org/10.1016/j.cattod.2016.06.020>.
 - [10] Y.L. Wei, K.W. Chen, H.P. Wang, Fe-modified TiO₂ nanocatalyst under blue-light irradiation, *J. Vac. Sci. Technol. B* 27 (2009) 1385–1387, <https://doi.org/10.1116/1.3079700>.
 - [11] J. Yu, Q. Xiang, M. Zhou, Preparation, characterization and visible-light-driven photocatalytic activity of Fe-doped titania nanorods and first-principles study for electronic structures, *Appl. Catal. B Environ.* 90 (2009) 595–602, <https://doi.org/10.1016/j.apcatb.2009.04.021>.
 - [12] H. Moradi, A. Eshaghi, S.R. Hosseini, K. Ghani, Fabrication of Fe-doped TiO₂ nanoparticles and investigation of photocatalytic decolorization of reactive red 198 under visible light irradiation, *Ultrason. Sonochem.* 32 (2016) 314–319, <https://doi.org/10.1016/j.ultsonch.2016.03.025>.
 - [13] S.U.M. Khan, M. Al-Shahry, W.B. Ingler, Efficient photochemical water splitting by a chemically modified n-TiO₂, *Science* 297 (2002) 2243–2245, <https://doi.org/10.1126/science.1075035>.
 - [14] A. Fujishima, T.N. Rao, D.A. Tryk, Titanium dioxide photocatalysis, *J. Photochem. Photobiol. C Photochem. Rev.* 1 (2000) 1–21, [https://doi.org/10.1016/S1389-5567\(00\)00002-2](https://doi.org/10.1016/S1389-5567(00)00002-2).
 - [15] C. Sotelo-Vazquez, N. Noor, A. Kafizas, R. Quesada-Cabrera, D.O. Scanlon, A. Taylor, J.R. Durrant, I.P. Parkin, Multifunctional P-doped TiO₂ Films: a new approach to self-cleaning, transparent conducting oxide materials, *Chem. Mater.* 27 (2015) 3234–3242, <https://doi.org/10.1021/cm504734a>.
 - [16] J. Li, D. Ren, Z. Wu, C. Huang, H. Yang, Y. Chen, H. Yu, Visible-light-mediated antifungal bamboo based on Fe-doped TiO₂ thin films, *RSC Adv.* 7 (2017) 55131–55140, <https://doi.org/10.1039/c7ra10103a>.
 - [17] G.N. Schrauzer, T.D. Guth, Photolysis of water and photoreduction of nitrogen on titanium dioxide, *J. Am. Chem. Soc.* 99 (1977) 7189–7193, <https://doi.org/10.1021/ja00464a015>.
 - [18] D.W. Bahnemann, Ultrasmall metal oxide particles: preparation, photo-physical characterization, and photocatalytic properties, *Isr. J. Chem.* 33 (1993) 115–136, <https://doi.org/10.1002/jjch.199300017>.
 - [19] W. Choi, A. Termin, M.R. Hoffmann, The role of metal ion dopants in quantum-sized TiO₂: correlation between photoreactivity and charge carrier recombination dynamics, *J. Phys. Chem.* 98 (1994) 13669–13679, <https://doi.org/10.1021/j100102a038>.
 - [20] K.T. Ranjit, I. Willner, S. Bossmann, A. Braun, Iron(III) phthalocyanine-modified titanium dioxide: a novel photocatalyst for the enhanced photo-degradation of organic pollutants, *J. Phys. Chem. B* 102 (1998) 9397–9403, <https://doi.org/10.1021/jp982694s>.
 - [21] S.J.A. Moniz, S.A. Shevlin, X. An, Z.-X. Guo, J. Tang, Fe₂O₃-TiO₂ Nanocomposites for enhanced charge separation and photocatalytic activity, *Chem. Eur. J.* 20 (2014) 15571–15579, <https://doi.org/10.1002/chem.201403489>.
 - [22] T. Ali, P. Tripathi, A. Azam, W. Raza, A.S. Ahmed, A. Ahmed, M. Muneer, Photocatalytic performance of Fe-doped TiO₂ nanoparticles under visible-light irradiation, *Mater. Res. Express* 4 (2017), 015022, <https://doi.org/10.1088/2053-1591/aa576d>.
 - [23] S. Ivanković, M. Gotić, M. Jurin, S. Musić, Photokilling squamous carcinoma cells SCCVII with ultrafine particles of selected metal oxides, *J. Sol. Gel Sci. Technol.* 27 (2003) 225–233, <https://doi.org/10.1023/A:1023715004575>.
 - [24] N. Nasralla, M. Yeganeh, Y. Astuti, S. Pitcharoenphun, N. Shahtahmasebi, A. Kompany, M. Karimipour, B.G. Mendis, N.R.J. Poolton, L. Siller, Structural and spectroscopic study of Fe-doped TiO₂ nanoparticles prepared by sol-gel method, *Sci. Iran.* 20 (2013) 1018–1022, <https://doi.org/10.1016/j.scient.2013.05.017>.
 - [25] M.V. Ganduglia-Pirovano, A. Hofmann, J. Sauer, Oxygen vacancies in transition metal and rare earth oxides: current state of understanding and remaining challenges, *Surf. Sci. Rep.* 62 (2007) 219–270, <https://doi.org/10.1016/j.surfrep.2007.03.002>.
 - [26] M. Hirano, T. Jōji, M. Inagaki, H. Iwata, Direct formation of iron(III)-doped titanium oxide (anatase) by thermal hydrolysis and its structural property, *J. Am. Ceram. Soc.* 87 (2004) 35–41, <https://doi.org/10.1111/j.1151-2916.2004.tb19941.x>.
 - [27] N. Uekawa, Y. Kurashima, K. Kakegawa, Y. Sasaki, Preparation and non-stoichiometric property of wide compositional Fe(III)-doped TiO₂ (anatase), *J. Mater. Res.* 15 (2000) 967–973, <https://doi.org/10.1557/JMR.2000.0138>.
 - [28] S. Yu, H.J. Yun, D.M. Lee, J. Yi, Preparation and characterization of Fe-doped TiO₂ nanoparticles as a support for a high performance CO oxidation catalyst, *J. Mater. Chem.* 22 (2012) 12629, <https://doi.org/10.1039/c2jm30360d>.
 - [29] R.I. Bickley, J.S. Lees, R.J.D. Tilley, L. Palmisano, M. Schiavell, Characterisation of iron/titanium oxide photocatalysts. Part 1.—structural and magnetic studies, *J. Chem. Soc., Faraday Trans.* 88 (1992) 377–383, <https://doi.org/10.1039/FT9928800377>.
 - [30] N. Sijaković-Vujčić, M. Gotić, S. Musić, M. Ivanda, S. Popović, Synthesis and microstructural properties of Fe-TiO₂ nanocrystalline particles obtained by a modified sol-gel method, *J. Sol. Gel Sci. Technol.* 30 (2004) 5–19.
 - [31] R.K. Hailstone, A.G. DiFrancesco, J.G. Leong, T.D. Allston, K.J. Reed, A study of lattice expansion in CeO₂ nanoparticles by transmission electron microscopy, *J. Phys. Chem. C* 113 (2009) 15155–15159, <https://doi.org/10.1021/jp903468m>.
 - [32] M. Gotić, S. Musić, Synthesis of nanocrystalline iron oxide particles in the iron(III) acetate/alcohol/acetic acid system, *Eur. J. Inorg. Chem.* 2008 (2008) 966–973, <https://doi.org/10.1002/ejic.200700986>.
 - [33] M. Gotić, G. Dražić, S. Musić, Hydrothermal synthesis of α-Fe₂O₃ nanorings with the help of divalent metal cations, Mn²⁺, Cu²⁺, Zn²⁺ and Ni²⁺, *J. Mol. Struct.* 993 (2011) 167–176, <https://doi.org/10.1016/j.molstruc.2010.12.063>.
 - [34] M. Gotić, G. Košćec, S. Musić, Study of the reduction and reoxidation of sub-stoichiometric magnetite, *J. Mol. Struct.* 924–926 (2009) 347–354, <https://doi.org/10.1016/j.molstruc.2008.10.048>.
 - [35] M. Gotić, S. Musić, Mössbauer, FT-IR and FE SEM investigation of iron oxides precipitated from FeSO₄ solutions, *J. Mol. Struct.* (2007) 834–836, <https://doi.org/10.1016/j.molstruc.2006.10.059>, 445–453.
 - [36] S. Musić, S. Popović, M. Gotić, Mössbauer spectroscopy and X-ray diffraction of oxide precipitates formed from FeSO₄ solution. Part II, *Croat. Chem. Acta* 60 (1987) 661–675.
 - [37] S. Musić, S. Popović, M. Gotić, Mössbauer spectroscopy and X-ray diffraction of oxide precipitates formed from FeSO₄ solution, *J. Mater. Sci.* 25 (1990) 3186–3190, <https://doi.org/10.1007/BF00587672>.
 - [38] M. Gotić, T. Jurkin, S. Musić, From iron(III) precursor to magnetite and vice versa, *Mater. Res. Bull.* 44 (2009) 2014–2021, <https://doi.org/10.1016/j.materresbull.2009.06.002>.
 - [39] G. Dražić, G. Štefanić, T. Jurkin, M. Gotić, Impact of cadmium and phosphate ions on the hematite nanorings formation, *J. Mol. Struct.* 1140 (2017) 113–121, <https://doi.org/10.1016/j.molstruc.2016.12.089>.
 - [40] M. Gotić, T. Jurkin, S. Musić, Factors that may influence the micro-emulsion synthesis of nanosize magnetite particles, *Colloid Polym. Sci.* 285 (2007) 793–800, <https://doi.org/10.1007/s00396-006-1624-2>.
 - [41] T. Jurkin, G. Štefanić, G. Dražić, M. Gotić, Synthesis route to δ-FeOOH nanodiscs, *Mater. Lett.* 173 (2016) 55–59, <https://doi.org/10.1016/j.matlet.2016.03.009>.
 - [42] K.A. Malini, M.R. Anantharaman, A. Gupta, Low temperature Mössbauer studies on magnetic nanocomposites, *Bull. Mater. Sci.* 27 (2004) 361–366, <https://doi.org/10.1007/BF02704773>.
 - [43] T. Ohsaka, F. Izumi, Y. Fujiki, Raman spectrum of anatase, TiO₂, *J. Raman Spectrosc.* 7 (1978) 321–324, <https://doi.org/10.1002/jrs.1250070606>.
 - [44] S.-H. Shim, T.S. Duffy, Raman spectroscopy of Fe₂O₃ to 62 GPa, *Am. Mineral.* 87 (2002) 318–326, <https://doi.org/10.2138/am-2002-2-314>.
 - [45] I.V. Chernyshova, M.F. Hochella, A.S. Madden, Size-dependent structural transformations of hematite nanoparticles. 1. Phase transition, *Phys. Chem. Chem. Phys.* 9 (2007) 1736–1750, <https://doi.org/10.1039/b618790k>.